Hysteresis-loop phenomena in disordered ferromagnets with demagnetizing field and finite temperature

Djordje Spasojević ⬡
Faculty of Physics, University of Belgrade, POB 44, 11001 Belgrade, Serbia

Sanja Janićević ⬡
Faculty of Science, University of Kragujevac, POB 60, 34000 Kragujevac, Serbia

Bosiljka Tadić ⬡
Department for Theoretical Physics, Jožef Stefan Institute, Sl-1001 Ljubljana, Slovenia

Using numerical simulations, we investigate the impact of the demagnetization field and finite temperature on the hysteresis phenomena in disordered ferromagnetics systems. We model the behavior of thin systems employing the thermal nonequilibrium random field Ising model driven by a finite-driving rate protocol to study the shape of the hysteresis loop and demagnetization line and the magnetization fluctuations for varied parameters. Our results reveal a significant interplay of the disorder, the demagnetizing fields, and thermal fluctuations. In particular, at a fixed disorder and temperature, the increasing demagnetization coefficient gradually prologues the magnetization reversal process, altering the multifractal nature of the magnetization fluctuations. The process accompanies the appearance of extended linear segments in the hysteresis loop and changes in the demagnetization line while practically preserving the value of the coercive field and slightly changing the remanent magnetization. On the other hand, increasing temperature expands the system's response fluctuations and narrows the loop, affecting the coercive field and remanent magnetization. The interplay of thermal fluctuations and demagnetizing fields fully manifests in limiting the large-scale magnetization fluctuations, revealed by the multifractal spectra and the scaling functions of the avalanches. Our research offers new modeling perspectives with a more realistic scenario and provides insight into new hysteresis loop phenomena relevant to theoretical analysis and applications.

I. INTRODUCTION

During magnetization and demagnetization processes disordered ferromagnetic materials display hysteresis behavior manifested by a hysteresis loop when the field is slowly changing during the magnetization reversal; these processes are accompanied by bursty (avalanching) response events manifested in the magnetization jumps measured as Barkhausen noise (BHN) signal [1]. Properties of the hysteresis loop, in particular, the coercivity and remanence (measuring the resistance to the demagnetization and the residual magnetization at the vanishing external field, respectively), as well as the structure of BHN, are crucial for various technological applications of these materials, for example, in memory and logic devices [2,3], or for assessing the microstructure of materials [4]. Another characterization of the states of the hysteresis loop is obtained by removing the finite magnetization through cycling loops of gradually smaller amplitude (i.e., subloops), until the zero magnetization is reached in the zero field [5]; these subloops' peaks define a characteristic demagnetization line of the sample [6].

Demagnetization of ferromagnetic systems has previously been investigated both theoretically and experimentally. Experimental research has been conducted revealing the role of demagnetizing effects on the avalanche statistics in Fe-Ni-Co alloys, Nd-Fe-B sintered magnets, and ferrite magnets [6,7]. In contrast, more current investigations concentrated on the demagnetizing field-induced magnetocaloric effect of commercial-grade Gd plates [8]. With the aid of magnetic shields, the development of magnetometers and sensors with increased sensitivity have resulted in several applications in medical and biomedical science in recent years [9,10]. Using the ultrafast optical demagnetization and sophisticated time-resolved magneto-optical Kerr effect (TRMOKE) measurements, the dynamics of magnetization in diverse magnetic structures was also examined [11–14]. In addition, thin and multilayer structures have received attention from experimental investigations due to their controllable magnetic properties and potential use as magnetic recording media [15,16]. For example, in multilayer magnetic nanostructures, superdiffusive spin transport has been experimentally proven as a new mechanism of ultrafast demagnetization [17].

In equilibrium statistical physics, the random field Ising model (RFIM) appears as a platform for investigating some fundamental questions related to critical phenomena in disordered systems; see Ref. [18] and references there. For example, some recent advances in this field concern the question of supersymmetry [19,20], the universality of the

critical behavior [21] and the finite-size scaling above the upper critical dimension [22]. Numerical simulations of the nonequilibrium (NEQ) athermal variant of RFIM [23–25], considered as a paradigmatic model for disordered ferromagnets, have revealed the occurrence of the nonequilibrium critical behavior of avalanches, elucidated by their finite-size scaling analysis [26–28], both in equilateral [27,29–38] and nonequilateral [39–43] system geometries. They also unveiled the unusual properties in the low disorder phase in the presence of a demagnetizing field where one would have expected the magnetization to have a significant jump. In contrast, the demagnetizing field interferes with the reversal process, resulting in a series of power-law distributed avalanches of different sizes with the cutoff regulated by the demagnetizing factor [44]. Previous studies of the low-field hysteresis near the demagnetized state in disordered ferromagnets have demonstrated that demagnetization is not achievable in the limit of weak disorder and that the Rayleigh law of hysteresis does not apply [45].

Standardly, numerous previous studies used the athermal (zero-temperature) NEQ RFIM model employing the adiabatic driving protocol in which the external field is constant during an avalanche propagation and then changed by the amount that triggers the least stable spin in the system. The closest modification is quasistatic driving where the external field is changed by a fixed amount ΔH between avalanches and kept constant during avalanches. A more realistic protocol, resembling an experimental situation, is the constant driving rate protocol where the external field is permanently changing regardless of the system activity. Recent systematic comparison of the experimental data for a nanocrystalline sample's Barkhausen noise with the results obtained by numerical simulations of athermal NEQ RFIM with finite-driving-rate protocol showed a remarkable agreement [46].

In this work, we expand the athermal NEQ RFIM approach to describe the simultaneous impact of the demagnetizing fields and finite temperatures on the hysteresis loop behavior in random ferromagnets. Specifically, we consider thin samples of disordered ferromagnets with open boundaries, driven at finite rates by the external magnetic field. We consider different strengths of the disorder estimated with respect to the critical disorder, which we have determined considering the same sample thickness in the athermal RFIM limit. We investigate the hysteresis loop behavior, particularly the shape of the saturation loop, subloops, and demagnetization line at varied temperatures and demagnetizing factors. Furthermore, we study the impact of these factors on the multiscale fluctuations of the magnetization (Barkhausen noise) and scaling features of the magnetization avalanches considering in particular conditions corresponding to low-temperature dynamics. By varying the system's parameters in a reasonable range, our results reveal a significant interplay of the disorder, demagnetizing field, and thermal fluctuations, leading to some new dynamical phenomena that can be scrutinized within the extended NEQ RFIM.

The paper is structured as follows. In Sec. II the details of the model are given. Section III shows the analysis of the shape of the hysteresis loop and demagnetization line by varied parameters. The effect of demagnetizing fields

on the structure of Barkhausen noise and system activity events is given in Sec. IV. The discussion and conclusion in Sec. V are followed by the two Appendixes A and B, giving more details on the flowchart of a single-run algorithm and a comparison with the behavior of the equilateral system, respectively.

II. EXTENDED RANDOM-FIELD ISING MODEL AND SIMULATIONS

In this paper, we study the system of Ising spins $s_i = \pm 1$ with the random field Ising model modified by including the long-ranged demagnetizing field. The spins are located at the sites i of a three-dimensional (i.e., 3D) thin cubic lattice (L, L, l), with quadratic base of linear size L and small thickness $l \ll L$. The spins are exposed to the external homogeneous magnetic field $\vec{H} = H\vec{e}$ that is parallel ($H > 0$), or antiparallel ($H < 0$) to the unit vector $\vec{e} = (e_1, e_2, e_3)$ specifying two possible spins' orientations (i.e., values) along $\vec{e}$: up ($s_i = +1$) or down ($s_i = -1$). The Hamiltonian of the considered system, containing L^2l spins, is given by

$$\mathcal{H} = -J \sum_{\langle ij \rangle} s_i s_j - H \sum_i s_i - \sum_i h_i s_i + \sum_i J_{\mathrm{D}} M s_i. \quad (1)$$

In its first term, $\langle ij \rangle$ marks the summation over nearest neighbors ferromagnetically coupled with the interaction strength J, set to $J = 1$ for simplicity. The second and third terms indicate the interaction of each spin s_i with the homogeneous external magnetic field H and a quenched random magnetic field h_i at site i, respectively. The values h_i are chosen independently at different lattice sites from the zero-mean Gaussian probability distribution $f(h) = \exp(-h^2/2R^2)/R\sqrt{2\pi}$, whose standard deviation R specifies the disorder strength in the system. The long-range demagnetizing field $-J_{\mathrm{D}}M$, implemented in the last term of Hamiltonian (1), is specified by an (effective) demagnetization field coefficient (factor) $J_{\mathrm{D}} \geqslant 0$ and the actual magnetization of the system $M = (\sum_i s_i)/N$. Therefore, each spin s_i is under the influence of the effective magnetic field

$$h_i^{\mathrm{eff}} = \sum_j s_j^{(i)} + H + h_i - J_{\mathrm{D}} M, \quad (2)$$

where $s_j^{(i)}$ are the nearest neighbors of s_i. During the field-driven magnetization reversal process simulated with the NEQ RFIM, the values of $s_j^{(i)}$, H, and M change in time, inducing the variations of the effective field h_i^{eff}. The spin $s_i(t)$ is considered to be field unstable at the moment t of (discrete) simulational time if the condition $s_i(t)h_i^{\mathrm{eff}}(t) < 0$ is fulfilled. In the athermal NEQ RFIM, all unstable spins will be flipped before the next moment $t + \Delta t$ (here with $\Delta t = 1$), while the field-stable spins, i.e., the spins for which $s_i(t)h_i^{\mathrm{eff}}(t) \geqslant 0$, will remain unchanged. We note that when $J_D > 0$, a back flipping of spins might occasionally occur due to the influence of the demagnetization field. On the other hand, when $J_D = 0$, such back flipping is impossible due to ferromagnetic coupling between the nearest neighbor spins at zero temperature.

In addition to the preceding field-stability testing, in the thermal (i.e., temperature $T > 0$) NEQ RFIM considered in

this work, the spins are also checked for thermal flipping. Given the spin-polarized states, we take that at each moment t a fraction $c = \Delta N/N$ of randomly selected spins are exposed to possible thermal flips [47]. Then a selected spin s_i will flip with the probability $p_i^{(\text{th})}$, where

$$p_i^{(\text{th})} = \frac{\exp\left(-s_i h_i^{\text{eff}}/T_r\right)}{\exp\left(-s_i h_i^{\text{eff}}/T_r\right) + \exp\left(s_i h_i^{\text{eff}}/T_r\right)}, \qquad (3)$$

is the (Boltzmann-type) probability of thermal flipping for spin s_i exposed to its effective field h_i^{eff}. Note that the parameter T_r stands for the relative temperature T/T_c where for the ferromagnetic sample $T_c = J$. Hence, for $s_i h_i^{\text{eff}} > 0$ it is likely (but not certain) that the selected spin s_i will be flipped, whereas for $s_i h_i^{\text{eff}} < 0$, the selected spin s_i has a small nonzero chance for flipping.

At each moment t, we change the value of H, perform the flipping tests, and subsequently change the orientation of all spins satisfying the flipping conditions. The magnetic field H is incremented (decremented) along the rising (falling) part of the hysteresis loop by the amount $\Delta H > 0$ specifying the driving rate $\Omega = \Delta H/\Delta t$ in the finite-driving-rate protocol adopted in this work. Such change of the driving field H, followed by the subsequent spin flips, perpetually modifies the effective field, which can induce a cascade of intermittent spin flipping to spread in time and space as an avalanche. In this type of driving, the simultaneously propagating avalanches may overlap in time and possibly merge in space, forming a system response named activity event [35].

Following the above-described rules, we simulate the system's evolution guided by the time-varying magnetic field, which drives the system along its saturated hysteresis loop and subsequently through a set of nested subloops shrinking to zero. The evolution along the rising part of the saturation hysteresis loop (i.e., the loop with magnetization ranging between $M = -1$ and $M = 1$) proceeds as follows: initially, all spins are with the same orientation (-1) and the external magnetic field has a significant negative value $H_{-\infty}$ providing that all spins are field stable. Then, the external magnetic field is increased in each time step until H reaches the value H_∞ such that all spins are $s_i = 1$ and field stable, completing the rising part of the saturation loop. After that, the simulation of the falling part of the saturation loop starts. To this end, H is decreased in each time step by ΔH until all spins are $s_i = -1$ and field stable when the simulation of the saturation loop falling part is completed.

After we finish the simulation of the whole saturation loop, we proceed to the simulation of the nested subloops. The magnetization of each (kth) subloop ranges between some maximum and minimum value, $H_k^{(\text{max})}$ and $H_k^{(\text{min})} = -H_k^{(\text{max})}$, of the external field, with $H_{k+1}^{(\text{max})} < H_k^{(\text{max})}$. The number of subloops and their range is selected in advance (as a sequence of fixed percentages of H_∞); the simulations follow the same steps as for the saturation loop, started, however, from the remembered spin state of the previous (sub)loop when H falls to $H^{(\text{min})}$ for that previous (sub)loop. Finally, the demagnetization curve is formed from the tips of all simulated (50 in our study) subloops. The entire single-run simulation procedure flowchart is given in Appendix A.
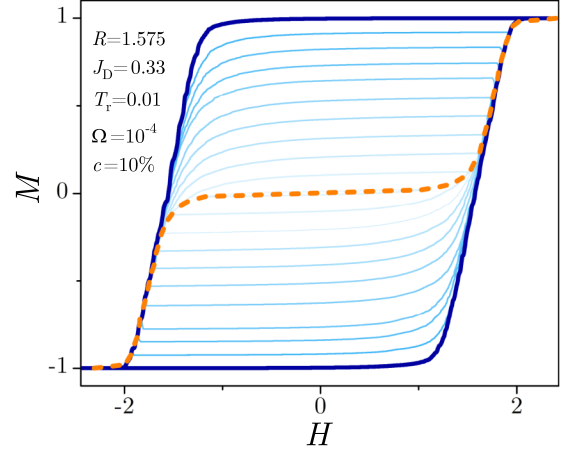

FIG. 1. Saturation hysteresis loop (full thick curve) with ten subloops (shown out of 50 by thin full curves) and the demagnetization (dashed) curve. System parameters are $L = 256$, $l = 4$, $R = 1.575$, $J_D = 0.33$, $T_r = 0.01$, $\Omega = 10^{-4}$, and $c = 10\%$.

III. PROPERTIES OF THE HYSTERESIS LOOP AND DEMAGNETIZATION CURVE BY VARIED PARAMETERS

This paper presents the results obtained in numerical simulations of the thermal NEQ RFIM with a demagnetizing field. Because many parameters influence the hysteresis-loop behavior, we show the results obtained when one parameter is varied while fixing the remaining parameters to their convenient or representative values.

The simulated systems contain a total of 262 144 spins arranged in a thin plate geometry with an equilateral base of linear size $L = 256$ and thickness $l = 4$. The demagnetization coefficient for (homogeneously magnetized) thin plates varies between 0 and 1 with the direction of the external field relative to the plate [48] ($J_D = 0$ for the field parallel to the base, and $J_D = 1$ for the field perpendicular to the base; showcased also in numerical simulations [49]). In Fig. 1, we first show the case of $J_D = 0.33$, which is also characteristic of the three-dimensional equilateral systems; for comparison, the results are shown in Appendix B. Then the results for a systematic variation of the parameters $J_D \in [0, 1]$ and $T_r \in [0.001, 10]$ are obtained, as shown in Figs. 2 and 3. The fraction of spins exposed to the thermal flipping, c, is varied within the range 10–50%.

Saturation hysteresis loops are cycled over up to 50 subloops. For the strength of disorder R, three representative values are considered: the subcritical ($R = 1.2 < R_c^{\text{eff}}$), supercritical ($R = 2.0 > R_c^{\text{eff}}$), and $R = 1.575$, which is approximately equal to the effective critical disorder $R_c^{\text{eff}}(L, L, l)$ estimated for the adiabatically driven athermal system situated on the same (L, L, l) cubic lattice, but with $J_D = 0$. In more details, for the adiabatically driven athermal infinite systems, the critical disorder R_c separates the supercritical domain of disorder $R > R_c$ (where all avalanches are finite) from the subcritical domain of disorder $R < R_c$ in which the phase transition of the first kind (i.e., jump in magnetization) appears due to the onset of infinite avalanche. In finite systems, the role of the infinite avalanche is played by the spanning avalanches, extending at least along one of
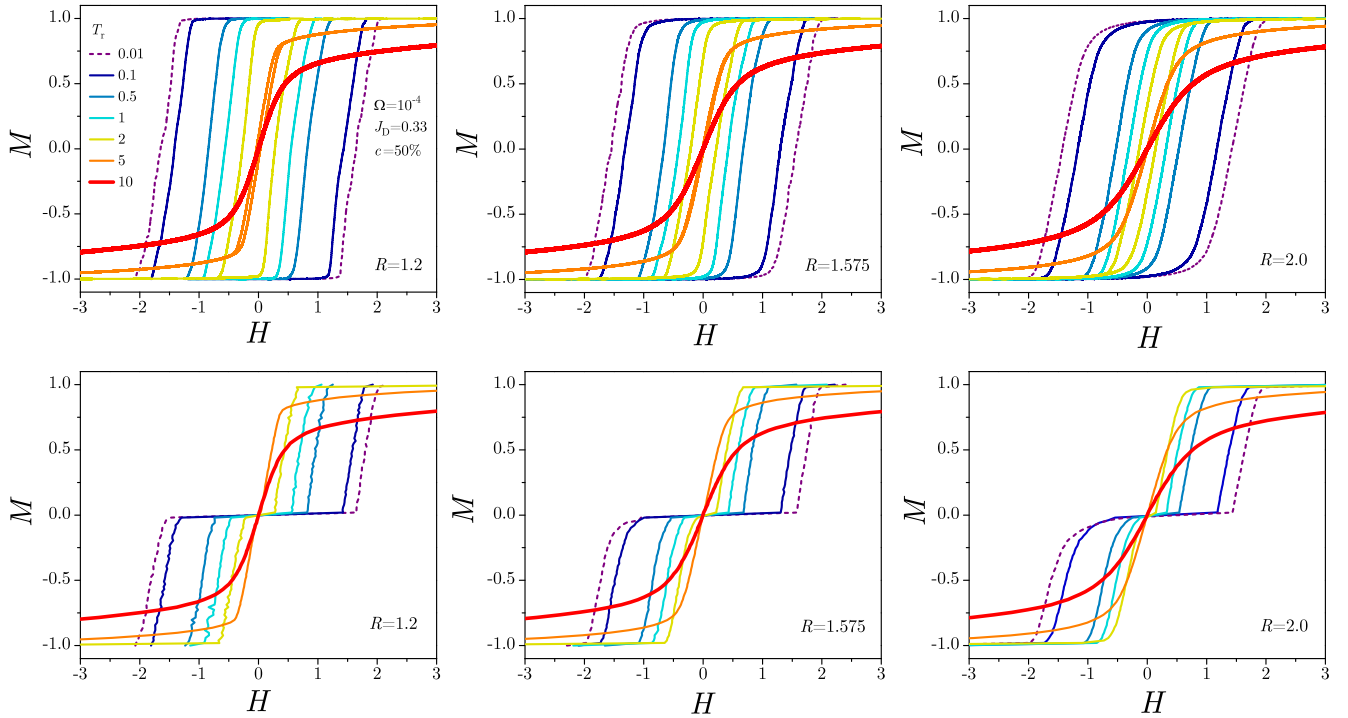
FIG. 2. The shrinking of single-run saturation magnetization curves with increasing relative temperature (top row) along with pertinent demagnetization curves (bottom row) obtained for systems with the same parameters $L = 256$, $l = 4$, $J_D = 0.33$, $\Omega = 10^{-4}$, $c = 50\%$, and disorder values shown in legends. The relative temperature is varied in the range $T_r = 0.01–10$ as is shown in the legend in the first and applicable to all panels.
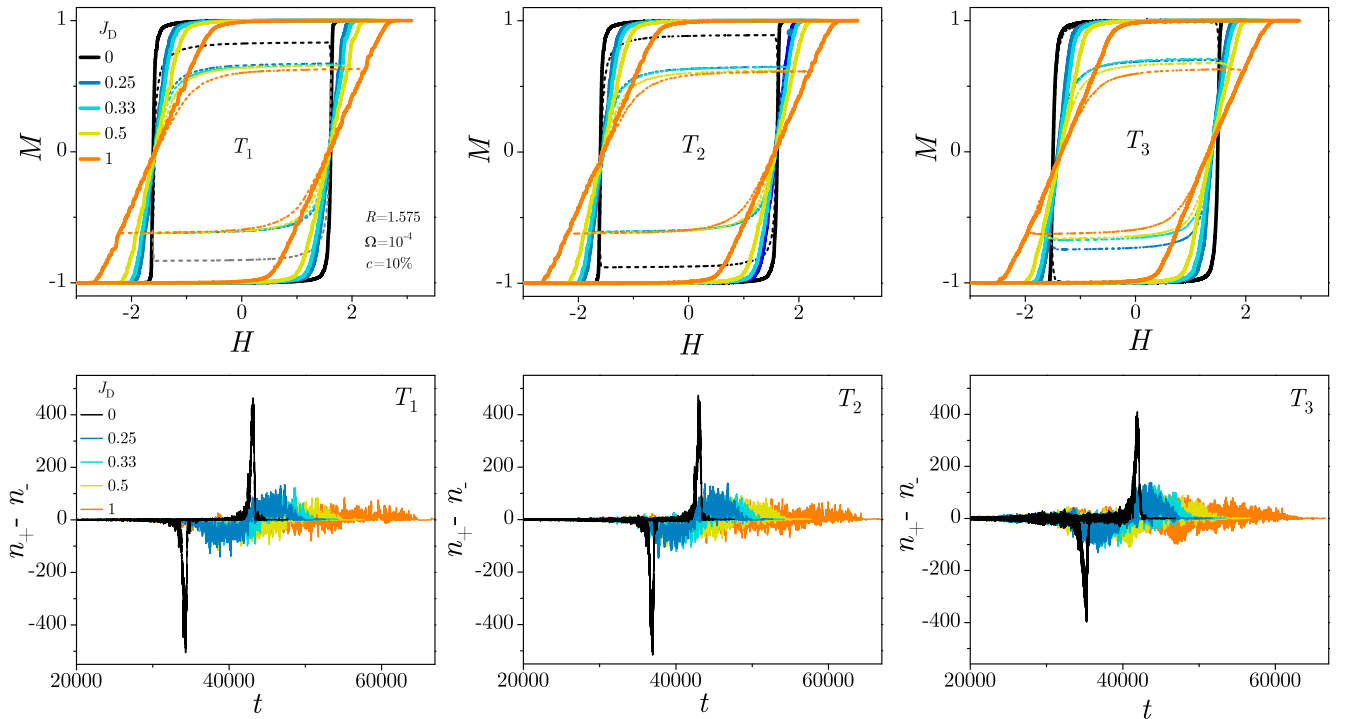

FIG. 3. Top row: Single-run magnetization loops for three values of relative temperature $T_1 = 0.001$, $T_2 = 0.01$, and $T_3 = 0.1$, the disorder value $R = 1.575$, $c = 10\%$, and a range of J_D values shown in the legend. Full lines show saturation curves, and the dashed ones, one representative subloop for each of the saturation loops. For $J_D = 0$ the saturation loops are (almost) rectangular (with rounded corners) becoming more and more tilted/slanted with the increase of J_D. Bottom row: Magnetization signals $n_+ - n_-$ vs simulation time t from the single-run simulations of the saturation loops shown in the top row; n_+ (n_-) is the number of spins flipped up (down) at a time step t. The results in all panels correspond to the $256 \times 256 \times 4$ system driven by the finite-driving-rate protocol with the driving rate $\Omega = 10^{-4}$. Legends in the first panels apply to all panels in the same row.

the system's dimensions [26,50,51]. For finite systems, such avalanches are likely (unlikely) for sufficiently low (high) disorders belonging to the subcritical (supercritical) domains of disorder separated by the domain of transitional disorders ($R_c < R < R_c^{\text{eff}}$), see Ref. [30], ending at some value R_c^{eff} named the effective critical disorder, which depends on the lattice geometry (L_x, L_y, L_z). So, for a finite system, the effective critical disorder is the minimal disorder such that the spanning avalanches are (statistically) absent for the system's lattice geometry. The effective critical disorder value is influenced not only by the lattice geometry but also by the driving rate Ω (particularly in the fast driving regime used in this work), as well as by the nonzero values of the T and J_D parameters. For (L, L, l) type lattices the theoretical prediction about dependence of R_c^{eff} on L, l for adiabatically driven athermal NEQ systems with $J_D = 0$ is given by Eq. (7) in Ref. [39] that is in agreement with the value $R_c^{\text{eff}}(256, 256, 4) = 1.575$ found in our simulations (for $T = 0$, $\Omega = 10^{-7}$, $J_D = 0$) and used in what follows. Note, however, that this value should be considered here merely as a representative value close to the effective critical disorder, while the other two considerably different chosen values, $R = 1.2$ and $R = 2.0$, are subcritical and supercritical for all employed values of J_D and T.

The system is driven using the finite-rate driving protocol with the driving rate $\Omega = 10^{-4}$, and open boundary conditions applied along all three axes.

A. Saturation magnetization loops, subloops, and demagnetization curves

Saturation magnetization loops are often prioritized in studies of ferromagnetic systems given that analysis of their shape and scaling behavior of avalanches provide substantial insights into the hysteresis-loop criticality [43,52,53]. On the other hand, the importance of hysteresis subloops also comes to light due to their intriguing properties (such as return point memory and history-induced critical scaling [23]), and also given the experimental challenges, e.g., the large magnetic fields required to push the magnetic samples to their saturation point.

For illustration, in Fig. 1, we show ten equally spaced subloops simulated for our system with disorder $R = 1.575$, demagnetizing factor $J_D = 0.33$ at low temperature and thermal activation fraction. The magnetization cycled through nested subloops when the external field, with a shrinking amplitude, swung back and forth. One can see that the shapes of the subloops resemble the shape of the saturation one while gradually decreasing in size upon decreasing the field amplitude. The dashed line in this figure shows the demagnetizing curve, defined as the line interconnecting the subloop tips [44].

B. Thermal effects on the hysteresis loop and demagnetization curve

To explore the effects of thermal fluctuations in the demagnetizing system, we have performed numerical simulations for several nonzero temperature values (relative to the system's critical temperature). The saturation hysteresis loops and related demagnetization curves as functions of the external magnetic field are displayed in Fig. 2. Thermal effects are studied in three distinct domains of disorder, more precisely, below, at and above the effective critical disorder $R_c^{\text{eff}}(L = 256, L = 256, l = 4) \approx 1.575$, estimated in the adiabatic and athermal limit. The relative temperature varies within a wide range $T_{\text{r}} = 0.01$–10. The demagnetizing coefficient is set to $J_D = 0.33$, which allows a comparison with the fully equilateral system of linear size $L = 64$, whose saturation magnetization curves varied over the same relative temperature range are shown in Fig. 8 of the Appendix B.

As can be seen in the top row of Fig. 2, the saturation magnetization loops exhibit a steep rise at the lower temperatures, especially in the low disorder domain (e.g., for $R = 1.2$); this feature is comparable to the athermal (i.e., $T = 0$) scenario. With the increase in temperature, we observe that the hysteresis loops for the three representative disorder values gradually narrow until it is virtually impossible to tell the difference between the rising and decreasing hysteresis branch (absence of hysteresis), and the coercive field tends to zero; in Ref. [54] they make a similar observation. The demagnetization curve's distinctive plateau, previously noted in the athermal case [44], persists in the range of lower temperatures. In the high-temperature range, it likewise contracts with the increase in temperature before dissolving, leading to a smooth demagnetization curve; see bottom row of Fig. 2.

Further, we focus on the impact of varied demagnetizing fields on the hysteresis loop and Barkhausen noise at low temperatures. We find that the dynamics of the system is greatly affected by the demagnetizing field, operating to counterbalance the external field and producing nonlocal long-range interactions among spins. In thin samples, the effective demagnetizing coefficient J_D can vary practically within the entire range $J_D \in [0, 1]$, depending on the domain structure and the direction of the external field [8]; meanwhile, a fixed value $J_D = 1/3$ is expected for a cubic sample with uniform magnetization [55]. The effects of the varied J_D values on the shape of the loops of the studied thin sample are illustrated in Fig. 3 for three representative relative temperatures. As the figure shows, the vertical parts of the hysteresis loops become gradually more inclined with increasing demagnetizing factor J_D; meanwhile, the coercivity and the remanent magnetization remain unchanged. The corresponding magnetization fluctuation $\delta M = n_+ - n_-$ is determined as the difference between the number of spins that flip up n_+ and down n_- at a time step t; the signals corresponding to the complete saturation loops are shown in the bottom row of Fig. 3. The shape of the corresponding subloop changes accordingly. The appearance of a sizable linear segment, previously also observed in Ref. [44], extends the central part of the hysteresis loop, which, in turn, prolongs the magnetization reversal process compared to the case without the demagnetizing fields.

IV. BARKHAUSEN NOISE AND ACTIVITY EVENTS AT VARIED DEMAGNETIZATION FACTOR AT LOW TEMPERATURES

In this section, we further demonstrate the interplay of the demagnetizing fields and temperature on the magnetization fluctuations (Barkhausen noise signals) by fixing the disorder, i.e., at the effective critical disorder estimated in the
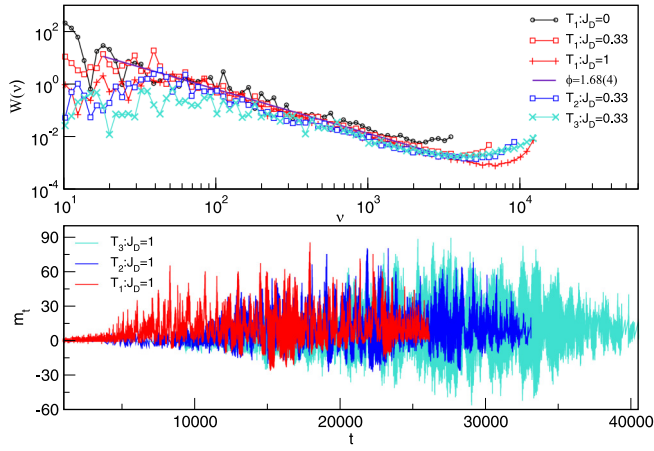
FIG. 4. Bottom panel: The magnetization-fluctuation signals for varied relative temperature $T_1 = 0.001$, $T_2 = 0.01$, $T_3 = 0.1$, fixed $J_D = 1$, $R = 1.575$, and $c = 10\%$. Top panel: Power spectra of the magnetization fluctuations for fixed temperature T_1 and three values of the demagnetization factor J_D, and for the fixed $J_D = 1$ and temperatures T_2 and T_3, as indicated in the legend.

adiabatically driven athermal simulations of the same thin sample. Specifically, we analyze the collective nature of these fluctuations on the ascending branch of the saturation loop by computing the signals' power spectra and multifractal features. In addition, the scale invariance of the magnetization activity events determined for varied disorders above the critical one is investigated. The results are reported in Figs. 4, 5, and 6.

In the presence of demagnetizing fields, back flips occur, reducing the magnetization, which leads to a prolonged reversal process compared to the case without demagnetizing fields ($J_D = 0$), even at very low temperatures. These effects cause differences in the left part of the power spectrum (low frequencies), thereby shifting the region where the power law is observed towards higher frequencies, cf. Fig. 4 top panel; meanwhile, the power-law exponent in $W(\nu) \sim \nu^{-\phi}$ remain relatively stable; we find $\phi = 1.68 \pm 0.04$, fitting the case with the low relative temperature $T_1 = 0.001$ and a moderate
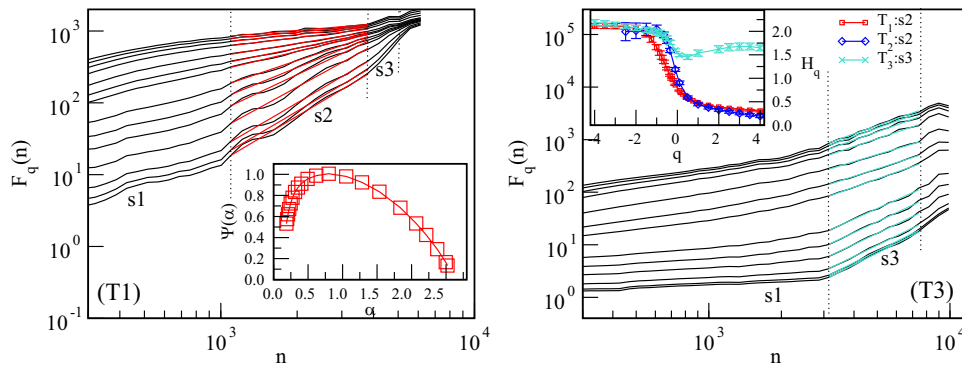

FIG. 6. Integrated distributions $D(S)$ of size S (circle symbols) and $D(T_{\mathrm{Dur}})$ of duration T_{Dur} (triangle symbols) of activity events for the system with parameters $L = 256$, $l = 4$, $J_D = 0.33$, $T_r = 0.01$, $\Omega = 10^{-4}$, $c = 10\%$, and (activity event detection) threshold region between -2 and 2, for a set of disorder values $R > R_c^{\mathrm{eff}}$. Presented data are averaged over 20 different realizations of random magnetic field. Insets show pertinent scaling collapses obtained for exponents $\tau_{\mathrm{int}} = 1.95 \pm 0.09$, $\alpha_{\mathrm{int}} = 2.60 \pm 0.02$, $\sigma = 0.98 \pm 0.04$, $\sigma\gamma = 1.01 \pm 0.03$, and $R_c^{\mathrm{eff}} = 1.575 \pm 0.108$, and having the collapse widths $w_{D(S)} = 0.108$ and $w_{D(T_{\mathrm{Dur}})} = 0.171$.

demagnetizing factor $J_D = 0.33$. However, a similar slope applies (albeit in a changed region) for all considered signals; see Fig. 4. Further elongation of the signal is caused by the increasing temperature, where thermal fluctuations also change the nature of the fluctuations, as described below. For example, Fig. 4, bottom panel shows three signals for a large $J_D = 1$ and different relative temperatures. In the following, their multifractal properties are analyzed to provide another quantitative measure of the altered nature of fluctuations.

We use the detrended multifractal analysis of time series [56] adapted for the study of sunspot time series in Ref. [57] and the Barkhausen noise in Ref. [58]. In this

FIG. 5. The main panels show the fluctuation function $F_q(n)$ vs segment length n for a large demagnetization factor $J_D = 1$, $R = 1.575$, $c = 10\%$, and very low relative temperature $T_1 = 0.001$, left, and a larger temperature $T_3 = 0.1$, right. The straight colored lines indicate fitted scaling regions, leading to the generalized Hurst exponent; symbols with the matching color are shown in the top right inset, in addition to H_q for $T_2 = 0.01$ case, determined in the section $s2$; see text. The corresponding singularity spectrum $\Psi(\alpha)$ vs α for the case T_1 is shown in the left panel inset.
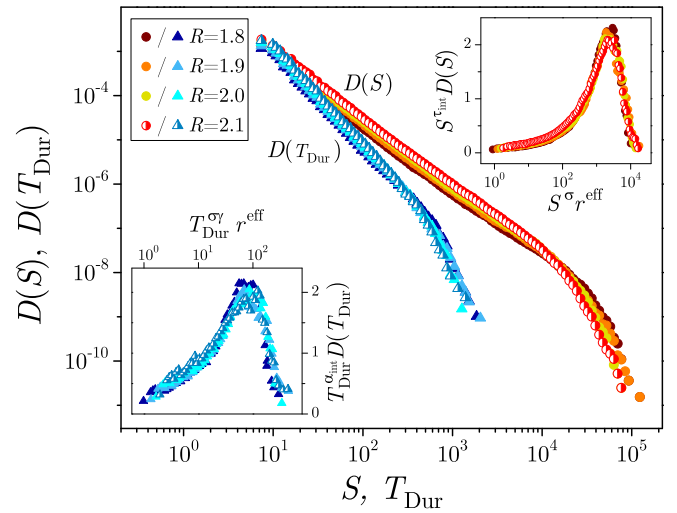
approach, for the considered magnetization fluctuation time series $\{m_t\}$, cf. Fig. 4, the profile $Y(i) = \sum_{t=1}^{i} (m_t - \langle m_t \rangle)$ is constructed and then divided into nonoverlapping segments of the length n, starting from the beginning of the time series; $N_s = \text{int}(N/n)$ intervals are defined, where N denotes the number of nonzero data points in the considered time series. Since the time series length is often not a multiple of the segment length n, the process is repeated starting from the endpoint, resulting in total of $2N_s$ intervals. With polynomial interpolation the local trend $y_\mu(i)$ is found at each segment μ, and standard deviation around it determined as $F^2(\mu, n) = \frac{1}{n} \sum_{i=1}^{n} \{Y[(\mu - 1)n + i] - y_\mu(i)\}^2$, for $\mu = 1, 2 \cdots N_s$. Similarly, starting from the endpoint, we get the expression $F^2(\mu, n) = \frac{1}{n} \sum_{i=1}^{n} \{Y[N - (\mu - N_s)n + i] - y_\mu(i)\}^2$ for $\mu = N_s + 1, \cdots 2N_s$. Using these expressions, the qth order fluctuation function

$$F_q(n) = \left\{ \frac{1}{2N_s} \sum_{\mu=1}^{2N_s} [F^2(\mu, n)]^{q/2} \right\}^{1/q} \sim n^{H_q} \qquad (4)$$

is determined as a function of the segment length varied in the range $n \in [2, N/4]$; for each value of the amplification factor q, here varied in the range $q \in [-4.5, 4.5]$, the fluctuation function $F_q(n)$ represents a separate line in the double-log plot in Fig. 5. Straight-line sections of these curves are fitted to determine the scaling exponents H_q, defined in (4). For a multifractal time series, parts with different singularities are amplified differently with positive or negative q values, leading to a broad spectrum of the generalized Hurst exponents H_q as a function of q. In contrast, lines for different q values are parallel in the case of monofractal time series. The singularity spectrum $\Psi(\alpha)$ is another quantitative measure of multifractal features; it can be obtained [56] from H_q by the Legendre transform $\Psi(\alpha) = q\alpha - \tau_q$, where $\tau_q = qH_q - 1$ is related to standard box-probability measure in partition function methods and $\alpha = d\tau_q/dq$. n this context, α determines the strength of singularity at a given data point in the time series, while $\Psi(\alpha)$ is the fractal dimension of the subset of data points with the singularity α.

In the studied examples, the fluctuation function $F_q(n)$ exhibits different multifractal features in specified sections of the time intervals n, indicated as $s1$, $s2$, and $s3$ in Fig. 5. Specifically, we observe the absence of scaling for small n; meanwhile, a broad spectrum H_q appears in the section $s2$ at low relative temperature T_1. The corresponding singularity spectrum is also shown in the inset to the left panel in Fig. 5. We observe an asymmetry characterized by a wide range of variations on the right side of the spectrum, which describes small magnetization fluctuations. Meanwhile, the left part of the spectrum, which is associated with large fluctuations, changes in a narrow range. The corresponding values of α, with the associated generalized Hurst exponent shown in the right panel inset, are in the range of a fractional Gaussian process. With the increasing temperature $T_2 = 0.01$, the segment $s2$ shrinks and eventually disappears at higher relative temperature $T_3 = 0.1$, where the scaling segment $s3$, corresponding to extensive time intervals, appears. Here, persistent large fluctuations lead to an entirely different type of the spectrum

with the Hurst exponent that exceeds one; see the inset in the right panel of Fig. 5.

Avalanching activity events are characterized by parameters such as the size S (number of spins flipped) and duration T_{Dur} (the time between the start and end of an event). The main panel of Fig. 6 shows the integrated distributions $D(S)$ and $D(T_{\text{Dur}})$ calculated from the events realized throughout the whole hysteresis loop. As can be seen, these distributions exhibit power-law segments, described by the associated critical exponents, ending with a cutoff region. According to the athermal and adiabatically driven version of RFIM [23], these distributions $D(S)$ and $D(T_{\text{Dur}})$, considered to be generalized homogeneous functions of their arguments, are expected to follow the scaling

$$D(S) = S^{-\tau_{\text{int}}} \mathcal{D}_S(S^\sigma r), \qquad (5)$$

$$D(T_{\text{Dur}}) = T_{\text{Dur}}^{-\alpha_{\text{int}}} \mathcal{D}_{T_{\text{Dur}}}(T_{\text{Dur}}^{\sigma\gamma} r), \qquad (6)$$

where $\mathcal{D}_S$ and $\mathcal{D}_{T_{\text{Dur}}}$ are the appropriate universal scaling functions and r the reduced disorder $r = (R - R_c)/R$ [R_c being the critical disorder of system in the thermodynamical limit ($L \to \infty$)]. Here, all the exponents are the standard RFIM ones, namely, τ_{int} and α_{int} are the size and duration exponents of integrated distributions (see Ref. [59]), σ is the cutoff exponent showing scaling of the largest size with the disorder, and γ the exponent describing the power-law correlation $\langle S \rangle_{T_{\text{Dur}}} \sim T_{\text{Dur}}^\gamma$ between the duration T_{Dur} and the mean size $\langle S \rangle_{T_{\text{Dur}}}$ of activity events having that duration, also shown to be equal to the power-spectrum exponent ϕ within the context of the athermal NEQ RFIM [60].

To find the values of related exponents, collapsing of the $D(S)$ and $D(T_{\text{Dur}})$ distributions is carried out in accordance with Eqs. (5) and (6), using the method that minimizes the collapse width w, the width of the region that contains scaled collapsing data (see Ref. [27], and the Appendix D in Ref. [32] for more details). Because there is always some extent of data scattering, the collapse width is always greater than zero, even for the optimal values of scaling parameters estimated so to minimize w and achieve the best possible overlay of the scaled data onto a single curve. Presenting the scaled data $S^{\tau_{\text{int}}} D(S)$ versus $S^\sigma r$, and $T_{\text{Dur}}^{\alpha_{\text{int}}} D(T_{\text{Dur}})$ versus $T_{\text{Dur}}^{\sigma\gamma} r$, corresponding to different disorders $R > R_c^{\text{eff}}$, one achieves the overlapping of pertinent distributions. Scaling collapses of the integrated avalanche size and duration distributions for our system with parameters $J_D = 0.33$, $T_r = 0.01$, $c = 10\%$, and (activity event detection) threshold region between -2 and 2, are presented in pertinent insets of Fig. 6. The best collapses are obtained for the following values of exponents: $\tau_{\text{int}} = 1.95 \pm 0.09$, $\alpha_{\text{int}} = 2.60 \pm 0.02$, $\sigma = 0.98 \pm 0.04$, and $\sigma\gamma = 1.01 \pm 0.03$, with the use of the effective reduced disorder $r^{\text{eff}} = (R - R_c^{\text{eff}})/R$ and $R_c^{\text{eff}} = 1.575 \pm 0.108$.

We see that the exponents τ_{int} and α_{int} agree within the error bars with those found for the fully 2D adiabatically driven athermal RFIM system, having values of $\tau_{\text{int}}^{2D} = 2.02 \pm 0.06$ and $\alpha_{\text{int}}^{2D} = 2.62 \pm 0.04$ [27,32]. These results align with those found for the thin system with the same base size $L = 256$, in which the 2D behavior is recovered for system thicknesses $l \leqslant 4$, followed by the two-slope distributions for $8 \leqslant l \leqslant 32$, and otherwise for thicknesses $l \geqslant 64$ displaying full 3D bulk behavior [43]. On the other hand, variations are observed in

the exponent values σ and γ. This discrepancy from the 2D values ($\sigma^{2D} = 0.10 \pm 0.01$ and $\gamma^{2D} = 1.55 \pm 0.03$ [27,32]) may be explained by the disparity in the effective critical disorder value as well as the strong mutual influence of the nonzero parameters J_D, T_r, and Ω, overriding the 2D framework.

V. DISCUSSION AND CONCLUSION

The hysteresis-loop phenomena depend on many factors such as the composition and preparation of the sample, degree of disorder, temperature, sample's shape, demagnetizing field, protocol of sample's driving by the external magnetic field, and the rate of field change. In this work, we have employed numerical simulations with an extended variant of the NEQ RFIM incorporating the impact of demagnetizing fields and thermal fluctuations on the hysteresis loop of a thin ferromagnetic sample.

The random character of the thermally activated spin flips tends to obstruct a precise detection of an avalanche, in contrast to athermal deterministic spin flips. Due to ubiquitous thermal fluctuations, the system's inactivity intervals are likely absent. For this reason, the detection of activity events (with potentially superposed thermal fluctuations) is accomplished through the introduction of a double-sided threshold region so that the system's response signal lying within this region is attributed to the sustained thermal activity, otherwise considered a field-related activity event. Due to the entangled field and thermal spin flipping, it is furthermore not realistic to keep the constant value of the external field during the ongoing activity event propagation. Hence, we have considered the constant rate of change of the external field.

While the probability of thermal flipping $p_i^{(th)}$ for a selected spin is usually taken in the form (3), a more intricate question regards the rate the spins are being selected. In a recent study of the thermal model [54], in a chosen number of time steps, the time of spin equilibration τ_{eq}, the spins are selected at random one at a time. After each thermal flip, the spin configuration is updated according to the field-activated flipping rule at the value of H, which is constant during τ_{eq}; then, the field is changed by an amount ΔH and the whole procedure iterated. In our computationally more efficient protocol, a given fraction c of spins is randomly selected and checked for thermal flipping at the current value of H. The remaining spins follow the field-flipping rule. These rules give more weight to the field flipping than thermal flipping, especially for small c, and are more suited to a low-temperature fixed point in the appropriate field-theory models [61]; meanwhile, the approach described in Refs. [54,62,63] is designed for the vicinity of the critical temperature. Interestingly, qualitatively similar conclusions are derived in both cases. Namely, the main effects of finite temperature consist of an overabundance of small activity events and hindering the propagation of massive avalanches. Meanwhile, the statistics of well-identified intermediate-range activity events are governed by the same scaling exponents as in the equivalent $T = 0$ dynamics.

The demagnetizing effect is another factor that significantly impacts the hysteresis loop dynamics. The demagnetizing field counteracts the external field inside the sample, introducing nonlocal interactions, limiting the size of underlying spin activity events and the maximum length of magnetization jumps [64]. Understanding its influence becomes crucial for applications and in many experimental investigations. In this context, the process of demagnetization has also been investigated as an alternative optimization tool, a way to determine the ground state of a disordered system [65,66] by comparison of the ground state of the RFIM with the demagnetized state, its nonequilibrium hysteretic counterpart, obtained by a sequence of slow magnetic-field oscillations with decreasing amplitude. The demagnetizing energy of a straight domain wall in a thin film with a perpendicular magnetic anisotropy was also calculated analytically, and verified by micromagnetic simulations [67].

In the studied model at finite temperature, we have systematically investigated the impact of demagnetizing fields on the nature of the magnetization fluctuations and system activity events. We find that while the values of the coercive field and remanent magnetization are virtually unchanged by the presence of demagnetizing fields, the increased demagnetizing coefficient changes the loop shape by introducing extended linear segments, corresponding to significantly prolonged magnetization or demagnetization processes. On the other hand, our analysis reveals that the hysteresis loop shape corresponding to a given disorder strength is altered by thermal fluctuations such that both coercivity and remanent magnetizations are decreasing. Note, however, that including the demagnetizing field is a sort of mean-field treatment of the magnetic dipole-dipole interaction. The actual demagnetizing field is constant over the entire sample only for the ellipsoidal ones; therefore, the demagnetizing factor J_D can be considered an effective quantity. For thin samples studied here, its value can be varied, theoretically, in the [0,1] range.

The presence of demagnetizing fields prolongs the magnetization reversal process and, at the same time, affects the nature of magnetization fluctuations, quantified by the multifractal time-series analysis of several representative Barkhausen noise signals. More precisely, demagnetizing fields mainly affect the large-scale fluctuations, resulting in the asymmetric singularity spectrum and shifting it towards smaller values of the singularity exponent α; cf. Fig. 5. Moreover, our results demonstrated the multiscale fractality. Specifically, different multifractal features occur in three segments of time intervals, roughly termed small, intermediate, and large, relative to the length of a given time series. The increasing temperature systematically alters the widths of these intervals and the shape of the associated generalized Hurst exponents spectra. In this way, our multifractal analysis reveals and quantifies an intricate interdependence of thermal fluctuations and demagnetizing effects in the magnetization fluctuations on the hysteresis loop.

With the considered driving rate and thermal fluctuations regarding low temperatures, we have conditions with the separation of the relevant time scales $\tau_{av} < \tau_{dr} \ll \tau_{th}$ of the avalanche propagation, driving, and thermalization, respectively [68]. In these conditions, we have successfully identified magnetization avalanches and studied their scaling features for different disorder strengths. The scaling collapse for both the distribution of the avalanche sizes and durations, shown in the insets of Fig. 6, demonstrate a
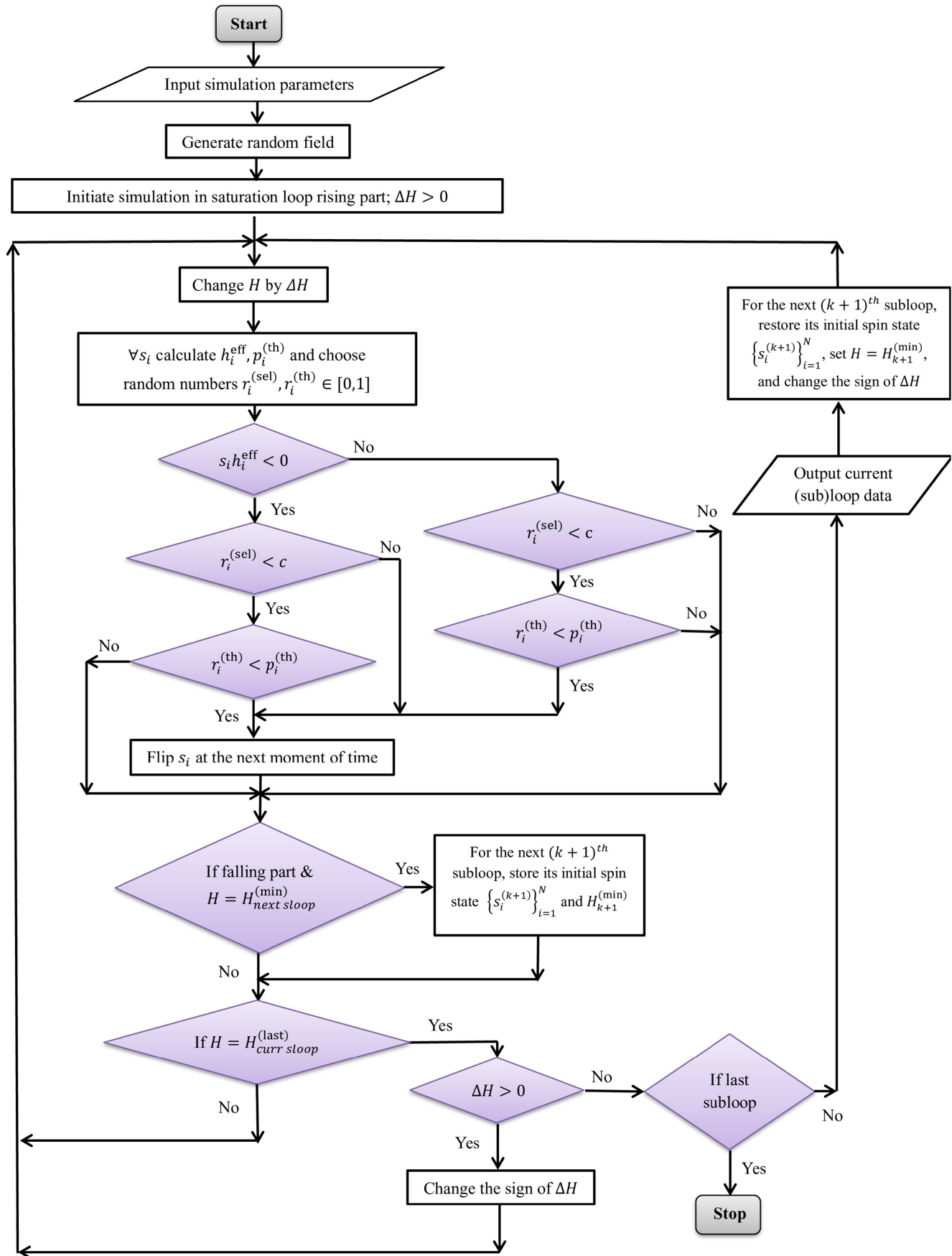
FIG. 7. A flowchart of the single-run algorithm used in our simulations.

characteristic asymmetry, theoretically predicted for the nonequilibrium critical dynamics by the renormalization group analysis in Ref. [61]. Meanwhile, the scaling exponents appear to be close (within error bars) to the ones observed in the athermal NEQ RFIM [27], supporting the idea of the RFIM universality [21]. A preliminary analysis of the avalanche collapse in the low disorder regime (not shown), suggests the occurrence of a new critical disorder and different exponents, potentially induced by the long-range effects of demagnetizing fields. Using a formal analogy with the model studied in Ref. [69], we may expect a new critical point to be associated with a self-organized criticality (SOC) on the hysteresis loop. The occurrence of SOC on the hysteresis loop was recently demonstrated in antiferromagnetic models on complex geometry [70] and earlier in the case of infinite-range spin-glass model [71]. These interesting aspects of the hysteresis-loop criticality in our extended NEQ RFIM are left for future study.

In conclusion, our work introduces a more realistic modeling approach for numerical investigations of the hysteresis loop phenomena in disordered ferromagnetic samples, thin films, and heterostructures, which are currently the focus of various applications. By appropriately extending the familiar approaches using the random field Ising model, our results revealed intricate interdependences of three factors often present in the experimental situation: the driving rate, thermal fluctuations, and demagnetizing fields and their impact on the hysteresis loop criticality. We have shown how these factors shape the hysteresis loop and the demagnetization line and change the multifractal features of the Barkhausen noise in these systems. Besides potential practical importance, the presented study opens several questions for future theoretical investigations in the context of out-of-equilibrium critical dynamics.

APPENDIX A: FLOWCHART OF A SINGLE-RUN ALGORITHM

In Fig. 7 we present the flowchart of a single-run algorithm used in our simulations of the RFIM version studied in this paper. Below is the explanation of some flowchart steps.

(1) The single-run simulation input parameters are: the size of the lattice (L, L, l) (setting the number of spins in the system $N = L^2 \times l$), the seed for the random number generator used in generating the configuration $\{h_i\}_{i=1}^N$ of the quenched random field, the disorder parameter R, the demagnetization field coefficient J_D, relative temperature T_r, the fraction of thermally flippable spins c, the value of ΔH (setting the driving rate $\Omega = \Delta H / \Delta t$), the number N_{sl} of subloops and the corresponding sequence $\{H_k^{(max)}\}_{k=1}^{N_{sl}}$ (setting

the maximum values of the external field H in each of the subloops).

(2) For the supplied value of seed, the (Gaussian) random field configuration $\{h_i\}_{i=1}^N$ is formed with the aid of the RNFARR procedure from Ref. [72] for generation of uniform deviates in (0,1) interval; the saturated hysteresis loop simulation is initialized by setting $s_i = -1$ for all spins and H to the maximum negative value such that all spins are field stable.

(3) In each (new) time step we first change the external field by ΔH.

(4) After H is changed, all spins are in parallel tested and (possibly) flipped through the following steps:

    (a) h_i^{eff} and p_i^{eff} are calculated for each s_i

    (b) random numbers $r_i^{(sel)}, r_i^{(th)} \in [0, 1]$ are generated for each i

    (c) for s_i that is:

      (i) field unstable, s_i is flipped

        (A) if $r_i^{(sel)} > c$ or

        (B) $(r_i^{(sel)} < c$ and $r_i^{(th)} < p_i^{eff})$

      (ii) field stable, s_i is flipped if $(r_i^{(sel)} < c$ and $r_i^{(th)} < p_i^{eff})$

(5) When $H < H_k^{(min)}$ for the first time on the falling part of the current kth (sub)loop, the initial spin state $\{s_i^{(k+1)}\}_{i-1}^N$ for the next (i.e., $k + 1$th) subloop is stored.

(6) After H falls below the $H_k^{(min)}$ for the first time on the falling part of the current (kth) (sub)loop, the simulation of the rising part of the next (i.e., $k + 1$th) subloop is initiated by restoring the spins to the initial spin configuration $\{s_i^{(k+1)}\}_{i-1}^N$ and H to $H_{k+1}^{(min)}$.

To perform quenched averaging, the foregoing single-run algorithm is repeated each time with a new configuration of the random field (initiated by a different value of the seed for the random number generator) and the same remaining input parameters.
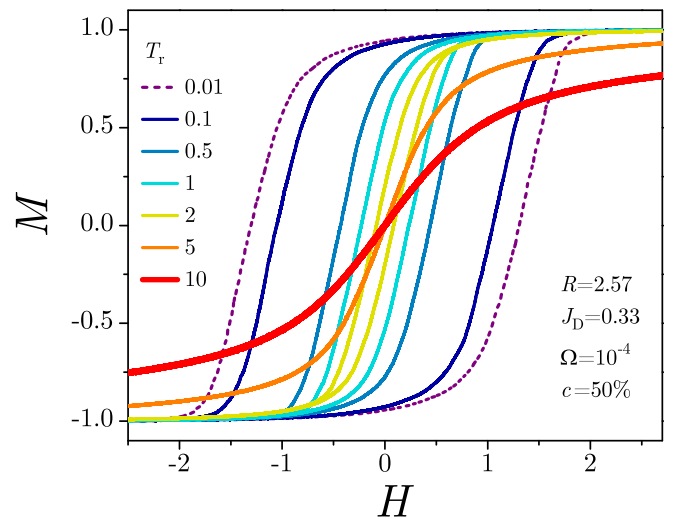

FIG. 8. The shrinking of single-run saturation magnetization curves with increasing temperature obtained for equilateral cubic system with parameters $L = 64$, $J_D = 0.33$, $\Omega = 10^{-4}$, $c = 50\%$. The relative temperature is varied in the range $T_r = 0.01–10$.

APPENDIX B: CASE OF EQUILATERAL SYSTEM

Determining the effects of demagnetization on the properties and behavior of the sample remains still a challenging task, particularly for nonellipsoidal forms. For instance, recent study conducted on cuboid systems [55] revealed temperature-dependent departures from the usual demagnetizing transformation, indicating inhomogeneous fields within the sample.

Here, in addition to the thin sample geometry examined in this work, we show how thermalization and presence of demagnetizing field affect the system with cubic geometry. By maintaining the same number of spins as in the thin system (total of 262 144 spins), we have conducted numerical simulations of the equilateral 3D cubic system with size $L = 64$. Thermal effects are examined in the domain of the effective critical disorder $R_c^{\mathrm{eff}}(L = 64) \approx 2.57$ estimated for the athermal case with adiabatic driving. With $c = 50\%$ as the fraction of thermally flippable spins, the relative temperature is varied throughout a broad range of values, from $T_r = 0.01$–10. The demagnetizing coefficient is set at $J_D = 0.33$, a value that corresponds to the homogeneously magnetized sample, and the system is driven with the same constant driving rate of $\Omega = 10^{-4}$.

Figure 8 shows the saturation hysteresis loops as functions of the external magnetic field. It is evident that the saturation magnetization loops show steep ascent at low temperatures, much like in the case of thin systems but with a milder transition to saturation values. As temperature rises, the width of hysteresis loops progressively narrows, eventually resulting in the overlapping of the rising and falling branches. This effect of ultimate hysteresis diminishing with temperature manifests at a lower relative temperature ($T_r = 5$) for the cubic than for the thin system ($T_r = 10$).

[1] D. C. Jiles and D. L. Atherton, Theory of ferromagnetic hysteresis, J. Magn. Magn. Mater. **61**, 48 (1986).

[2] S. Parkin, M. Hayashi, and L. Thomas, Magnetic domain-wall racetrack memory, Science **320**, 190 (2008).

[3] D. A. Allwood, G. Xiong, C. C. Faulkner, D. Atkinson, D. Petit, and R. P. Cowburn, Magnetic domain-wall logic, Science **309**, 1688 (2005).

[4] J. Jiao, Y. Chang, S. Kobayashi, X. Liu, G. Li, B. Wu, and C. He, Experimental evaluation and theoretical analysis of the mechanical properties of ferromagnetic materials using the magnetic hysteresis properties, J. Magn. Magn. Mater. **554**, 169310 (2022).

[5] M. Pitoňák, N. Ganev, K. Zgútová, J. Čapek, M. Neslušan, and K. Trojan, Influence of demagnetization and microstructure non-homogeneity on Barkhausen noise in the high-strength low-alloyed steel 1100 MC, Appl. Sci. **14**, 1511 (2024).

[6] J. S. Urbach, R. C. Madison, and J. T. Markert, Interface depinning, self-organized criticality, and the Barkhausen effect, Phys. Rev. Lett. **75**, 276 (1995).

[7] Y. Matsuura, K. Ishigami, R. Tamura, and T. Nakamura, Demagnetization processes of Nd-Fe-B sintered magnets and ferrite magnets as demonstrated by soft X-ray magnetic circular dichroism microscopy, J. Magn. Magn. Mater. **579**, 170854 (2023).

[8] Q. Badosa, L. Mañosa, E. Vives, A. Planes, B. Weise, L. Beyer, and E. Stern-Taulats, Demagnetizing field-induced magnetocaloric effect in Gd, J. Appl. Phys. **134**, 113902 (2023).

[9] H. Kikuchi, S. Kamata, T. Nakai, S. Hashi, and K. Ishiyama, Influence of demagnetizing field on thin-film GMI magnetic sensor elements with uniaxial magnetic anisotropy, Sens. Actuators, A **230**, 142 (2015).

[10] J. Yang, M. Shi, X. Zhang, Y. Ma, Y. Liu, S. Yuan, and B. Han, Demagnetization parameters evaluation of magnetic shields based on anhysteretic magnetization curve, Materials **16**, 5238 (2023).

[11] X. Chen, R. Adam, F. Wang, Y. Song, L. Pan, C. Song, S. Heidtfeld, C. Greb, Q. Li, J. Yu, J. Zhang, Y. Cui, S. Li, J. Xu, M. Cinchetti, C. Schneider, and D. Cao, Magnetic domain-dependent ultrafast optical demagnetization in stripe domain films, J. Phys. D **56**, 285001 (2023).

[12] W. Zhang, T. Blank, C. Guillemard, C. de Melo, S. Mangin, A. Kimel, S. Andrieu, and G. Malinowski, Ultrafast demagnetization of Co$_2$MnSi$_{1-x}$Al$_x$ Heusler compounds using terahertz and infrared light, Phys. Rev. B **107**, 224408 (2023).

[13] Z. Xie, Y. Cai, M. Tang, J. Zhou, J. Liu, J. Peng, T. Jiang, Z. Shi, and Z. Chen, Fluence and temperature dependences of laser-induced ultrafast demagnetization and recovery dynamics in $L1_0$-FePt thin film, Materials **16**, 5086 (2023).

[14] Z. Gong, W. Zhang, J. Liu, Z. Xie, X. Yang, J. Tang, H. Du, N. Li, X. Zhang, W. He, and Z.-h. Cheng, Ultrafast demagnetization dynamics in the epitaxial FeGe(111) film chiral magnet, Phys. Rev. B **107**, 144429 (2023).

[15] J. E. Davies, O. Hellwig, E. E. Fullerton, and K. Liu, Temperature-dependent magnetization reversal in (Co/Pt)/Ru multilayers, Phys. Rev. B **77**, 014421 (2008).

[16] A. Berger, C. Binek, D. T. Margulies, A. Moser, and E. E. Fullerton, Reversible hysteresis loop tuning, Phys. B: Condens. Matter **372**, 168 (2006), Proceedings of the Fifth International Symposium on Hysteresis and Micromagnetic Modeling.

[17] T. Jiang, X. Zhao, Z. Chen, Y. You, T. Lai, and J. Zhao, Ultrafast dynamics of demagnetization in FeMn/MnGa bilayer nanofilm structures via phonon transport, Nanomaterials **12**, 4088 (2022).

[18] S. Rychkov, *Lectures on the Random Field Ising Model: From Parisi-Sourlas Supersymmetry to Dimensional Reduction*, Springer Briefs in Physics (Springer, Berlin, 2023).

[19] N. G. Fytas, V. Martín-Mayor, G. Parisi, M. Picco, and N. Sourlas, Evidence for supersymmetry in the random-field Ising model at $D = 5$, Phys. Rev. Lett. **122**, 240603 (2019).

[20] A. Kaviraj, S. Rychkov, and E. Trevisani, Parisi-sourlas supersymmetry in random field models, Phys. Rev. Lett. **129**, 045701 (2022).

[21] N. Fytas, and V. Martín-Mayor, Universality in the three-dimensional random-field Ising model, Phys. Rev. Lett. **110**, 227201 (2013).

[22] N. G. Fytas, V. Martín-Mayor, G. Parisi, M. Picco, and N. Sourlas, Finite-size scaling of the random-field Ising model

above the upper critical dimension, Phys. Rev. E **108**, 044146 (2023).

[23] J. P. Sethna, K. A. Dahmen, and O. Perković, *The Science of Hysteresis*, edited by G. Bertotti and I. Mayergoyz (Academic Press, Amsterdam, 2006).

[24] D. P. Belanger, Experiments on the random field Ising model, *Spin Glasses and Random Fields*, edited by A. P. Young (World Scientific, Singapore, 1997), pp. 251–275.

[25] T. Natterman, Theory of the random field Ising model, *Spin Glasses and Random Fields*, edited by A. P. Young (World Scientific, Singapore, 1997), pp. 277–298.

[26] F. J. Pérez-Reche and E. Vives, Finite-size scaling analysis of the avalanches in the three-dimensional Gaussian random-field Ising model with metastable dynamics, Phys. Rev. B **67**, 134421 (2003).

[27] D. Spasojević, S. Janićević, and M. Knežević, Numerical evidence for critical behavior of the two-dimensional nonequilibrium zero-temperature random field Ising model, Phys. Rev. Lett. **106**, 175701 (2011).

[28] S. Mijatović, D. Jovković, S. Janićević, S. Graovac, and D. Spasojević, A tool for identifying the criticality in the disordered systems with metastable dynamics, Physica A **572**, 125883 (2021).

[29] O. Perković, K. A. Dahmen, and J. P. Sethna, Disorder-induced critical phenomena in hysteresis: Numerical scaling in three and higher dimensions, Phys. Rev. B **59**, 6106 (1999).

[30] S. Janićević, D. Knežević, S. Mijatović, and D. Spasojević, Scaling domains in the nonequilibrium athermal random field Ising model of finite systems, J. Stat. Mech.: Theory Exp. (2021) 013202.

[31] S. Graovac, S. Mijatović, and D. Spasojević, Mechanism of subcritical avalanche propagation in three-dimensional disordered systems, Phys. Rev. E **103**, 062123 (2021).

[32] D. Spasojević, S. Janićević, and M. Knežević, Avalanche distributions in the two-dimensional nonequilibrium zero-temperature random field Ising model, Phys. Rev. E **84**, 051119 (2011).

[33] S. Janićević, S. Mijatović, and D. Spasojević, Critical behavior of the two-dimensional nonequilibrium zero-temperature random field Ising model on a triangular lattice, Phys. Rev. E **95**, 042131 (2017).

[34] S. Mijatović, D. Jovković, and D. Spasojević, Nonequilibrium athermal random-field Ising model on hexagonal lattices, Phys. Rev. E **103**, 032147 (2021).

[35] S. Radić, S. Janićević, D. Jovković, and D. Spasojević, The effect of finite driving rate on avalanche distributions, J. Stat. Mech.: Theory Exp. (2021) 093301.

[36] D. Spasojević and S. Janićević, Two-dimensional ferromagnetic systems with finite driving, Chaos Soliton Fract. **158**, 112033 (2022).

[37] D. Spasojević, S. Radić, D. Jovković, and S. Janićević, Spin activity correlations in driven disordered systems, J. Stat. Mech.: Theory Exp. (2022) 063302.

[38] D. Spasojević, S. Graovac, and S. Janićević, Interplay of disorder and type of driving in disordered ferromagnetic systems, Phys. Rev. E **106**, 044107 (2022).

[39] D. Spasojević, S. Mijatović, V. Navas-Portella, and E. Vives, Crossover from three-dimensional to two-dimensional

systems in the nonequilibrium zero-temperature random-field Ising model, Phys. Rev. E **97**, 012109 (2018).

[40] S. Mijatović, M. Branković, S. Graovac, and D. Spasojević, Avalanche properties in striplike ferromagnetic systems, Phys. Rev. E **102**, 022124 (2020).

[41] S. Mijatović, D. Jovković, S. Janićević, and D. Spasojević, Critical disorder and critical magnetic field of the nonequilibrium athermal random-field Ising model in thin systems, Phys. Rev. E **100**, 032113 (2019).

[42] B. Tadić, Dynamical implications of sample shape for avalanches in 2-dimensional random-field Ising model with saw-tooth domain wall, Physica A **493**, 330 (2018).

[43] B. Tadić, S. Mijatović, S. Janićević, D. Spasojević, and G. J. Rodgers, The critical Barkhausen avalanches in thin random-field ferromagnets with an open boundary, Sci. Rep. **9**, 6340 (2019).

[44] J. Carpenter and K. Dahmen, Barkhausen noise and critical scaling in the demagnetization curve, Phys. Rev. B **67**, 020412(R) (2003).

[45] L. Dante, G. Durin, A. Magni, and S. Zapperi, Low-field hysteresis in disordered ferromagnets, Phys. Rev. B **65**, 144441 (2002).

[46] D. Spasojević, M. Marinković, D. Jovković, S. Janićević, L. Laurson, and A. Djordjević, Barkhausen noise in disordered striplike ferromagnets: Experiment versus simulations, Phys. Rev. E **109**, 024110 (2024).

[47] The fraction c regulates the amount of incessant thermal spin-flipping attempts between two successive discrete changes of the external magnetic field, thus playing a similar role to the number of Monte Carlo steps in Ref. [54]. Two independent parameters, $c < 1$ and T_r, enable us better control of the time scale separation, maintaining the system close to the disorder-dominated fixed point at low temperatures, where thermal fluctuations are subordinate to the driving and avalanche spreading dynamics studied in this paper. Our algorithm allows the limit $c = 1$ with fully developed thermal fluctuations near the temperature-dominated fixed point.

[48] D. Pozar, *Microwave Engineering* (John Wiley and Sons, New York, 1998).

[49] C. R. H. Bahl, Estimating the demagnetization factors for regular permanent magnet pieces, AIP Adv. **11**, 075028 (2021).

[50] F. J. Pérez-Reche and E. Vives, Spanning avalanches in the three-dimensional Gaussian random-field Ising model with metastable dynamics: Field dependence and geometrical properties, Phys. Rev. B **70**, 214422 (2004).

[51] D. Spasojević, S. Janićević, and M. Knežević, Analysis of spanning avalanches in the two-dimensional nonequilibrium zero-temperature random-field Ising model, Phys. Rev. E **89**, 012118 (2014).

[52] S. Mijatović, S. Graovac, D. Spasojević, and B. Tadić, Tuneable hysteresis loop and multifractal oscillations of magnetisation in weakly disordered antiferromagnetic - ferromagnetic bilayers, Physica E **142**, 115319 (2022).

[53] D. Spasojević, S. Mijatović, and S. Janićević, Dimensional crossover in driving-rate induced criticality on the hysteresis-loop of disordered ferromagnetic systems, J. Stat. Mech.: Theory Exp. (2023) 033210.

[54] L. Yao and R. T. L. Jack, Thermal vestiges of avalanches in the driven random field Ising model, J. Stat. Mech.: Theory Exp. (2023) 023303.

[55] M. Twengström, L. Bovo, O. A. Petrenko, S. T. Bramwell, and P. Henelius, LiHoF$_4$: Cuboidal demagnetizing factor in an ising ferromagnet, Phys. Rev. B **102**, 144426 (2020).

[56] J. W. Kantelhardt, S. A. Zschiegner, E. Koscielny-Bunde, S. Havlin, A. Bunde, and H. E. Stanley, Multifractal detrended fluctuation analysis of nonstationary time series, Physica A **316**, 87 (2002).

[57] M. Sadegh Movahed, G. Jafari, F. Ghasemi, S. Rahvar, and M. R. R. Tabar, Multifractal detrended fluctuation analysis of sunspot time series, J. Stat. Mech.: Theory Exp. (2006) P02003.

[58] B. Tadić, Multifractal analysis of Barkhausen noise reveals the dynamic nature of criticality at hysteresis loop, J. Stat. Mech.: Theory Exp. (2016) 063305.

[59] $\tau_{\text{int}} = \tau + \sigma\beta\delta$, $\alpha_{\text{int}} = \alpha + \beta\delta/\nu z$, and $\gamma = 1/\sigma\nu z$, where τ and α are the corresponding exponents for the distributions of avalanche size and duration collected in a narrow window of the external magnetic field [23]. Next, ν is the correlation length exponent, z is the dynamical critical exponent that describes scaling $T_{\text{Dur}} \sim l^z$ between avalanche of linear size l and avalanche duration, β pertains to scaling $\Delta M \sim |r|^\beta$ of the magnetization jump $\Delta M = M - M_c$ below R_c, δ to the scaling $\hat{m}_R^{\text{eff}} \sim (\hat{h}_R^{\text{eff}})^{1/\delta}$ of the effective reduced magnetization $\hat{m}_R^{\text{eff}} = M_R(H) - M_c^{\text{eff}}(R)$ with effective reduced magnetic field $\hat{h}_R^{\text{eff}} = H - H_c^{\text{eff}}(R)$ at $R = R_c$, see in Ref. [30] where $M_c^{\text{eff}}(R)$ and $H_c^{\text{eff}}(R)$ are the effective critical magnetization and the effective critical field at disorder R.

[60] M. Kuntz and J. Sethna, Noise in disordered systems: The power spectrum and dynamic exponents in avalanche models, Phys. Rev. B **62**, 11699 (2000).

[61] I. Balog, G. Tarjus, and M. Tissier, Criticality of the random field Ising model in and out of equilibrium: A nonperturbative functional renormalization group description, Phys. Rev. B **97**, 094204 (2018).

[62] F. Ettori, F. Perani, S. Turzi, and P. Biscari, Finite-temperature avalanches in 2D disordered Ising models, J. Stat. Phys. **190**, 89 (2023).

[63] M. Metra, L. Zorrilla, M. Zani, E. Puppin, and P. Biscari, Temperature-dependent criticality in random 2D Ising models, Europhys. J. Plus **136**, 939 (2021).

[64] G. Durin and S. Zapperi, The Barkhausen effect, *The Science of Hysteresis*, edited by G. Bertotti and I. D. Mayergoyz (Academic Press, Oxford, 2006), pp. 181–267.

[65] S. Zapperi, F. Colaiori, L. Dante, V. Basso, G. Durin, A. Magni, and M. J. Alava, Is demagnetization an efficient optimization method? J. Magn. Magn. Mater. **272–276**, E1009 (2004), Proceedings of the International Conference on Magnetism (ICM 2003).

[66] M. J. Alava, V. Basso, F. Colaiori, L. Dante, G. Durin, A. Magni, and S. Zapperi, Ground-state optimization and hysteretic demagnetization: The random-field Ising model, Phys. Rev. B **71**, 064423 (2005).

[67] A. Skaugen, P. Murray, and L. Laurson, Analytical computation of the demagnetizing energy of thin-film domain walls, Phys. Rev. B **100**, 094440 (2019).

[68] F.-J. Pérez-Reche, B. Tadić, L. Mañosa, A. Planes, and E. Vives, Driving rate effects in avalanche-mediated first-order phase transitions, Phys. Rev. Lett. **93**, 195701 (2004).

[69] F.-J. Pérez-Reche, L. Truskinovsky, and G. Zanzotto, Driving-induced crossover: From classical criticality to self-organized criticality, Phys. Rev. Lett. **101**, 230601 (2008).

[70] B. Tadić and R. Melnik, Fundamental interactions in self-organised critical dynamics on higher order networks, Eur. Phys. J. B **97**, 68 (2024).

[71] F. Pázmándi, G. Zaránd, and G. T. Zimányi, Self-organized criticality in the hysteresis of the Sherrington-Kirkpatrick model, Phys. Rev. Lett. **83**, 1034 (1999).

[72] D. Knuth, *The Art of Computer Programming, Seminumerical Algorithms*, 3rd ed. (Addison-Wesley Longman, Boston, 1997), Vol. 2.